Variational density-functional perturbation theory for dielectrics and lattice dynamics

Keith Refson*
Rutherford Appleton Laboratory, Chilton, Didcot, Oxfordshire OX11 0QX, United Kingdom

Paul R. Tulip† and Stewart J. Clark‡
Department of Physics, The University of Durham, Science Laboratories, South Road, Durham DH1 3LE, United Kingdom
(Received 4 October 2005; revised manuscript received 2 December 2005; published 19 April 2006)

The application of variational density functional perturbation theory (DFPT) to lattice dynamics and dielectric properties is discussed within the plane-wave pseudopotential formalism. We derive a method to calculate the linear response of the exchange-correlation potential in the GGA at arbitrary wavevector. We introduce an efficient self-consistent solver based on all-bands conjugate-gradient minimization of the second order energy, and compare the performance of preconditioning schemes. Lattice-dynamical and electronic structure consequences of space-group symmetry are described, particularly their use in reducing the computational effort required. We discuss the implementation in the CASTEP DFT modeling code, and how DFPT calculations may be efficiently performed on parallel computers. We present results on the lattice dynamics and dielectric properties of α-quartz, the hydrogen bonded crystal $NaHF_2$ and the liquid-crystal-forming molecule 5CB. Excellent agreement is found between theory and experiment within the GGA.

DOI: 10.1103/PhysRevB.73.155114 PACS number(s): 71.10.−w, 63.20.−e

I. INTRODUCTION

Density-functional theory[1,2] (DFT) has become the most commonly used methodology of calculating accurately the physical properties of a vast range of materials. Density-functional perturbation theory[3,4] (DFPT) extends the scope of the DFT Hamiltonian to allow the *ab initio* calculation of lattice dynamics and response to external electromagnetic fields. First-order DFPT yields the linear response of the Kohn-Sham orbitals with respect to the external perturbation and the second-order response of the energy by virtue of the so-called "$2n+1$ theorem."[5]

Many experimentally determined quantities are (often second-order) responses of the total energy of the system with respect to some perturbation. For example, derivatives of energy with respect to atomic position give vibrational frequencies, derivatives with respect to applied electric field give molecular polarizability or dielectric permittivities, and magnetic fields lead to nuclear magnetic resonance chemical shifts and magnetic susceptibilities. It is sometimes possible to calculate a response using a finite-difference approach to obtain the necessary derivatives. However this method fails when trying to compute the response to an incommensurate phonon wave vector or a finite electric field in a periodic solid. Obtaining these responses motivated the developments in DFPT which is able to treat an incommensurate perturbation using only a primitive-cell calculation and the response to an infinitesimal electric field. Combined, these perturbations contain all of the physics necessary for a complete *ab initio* treatment of lattice dynamics in the harmonic approximation including the effect of long-range electric fields which couple with longitudinal phonon modes giving rise to the well-known phenomenon of LO-TO splitting.

Significant advances in the formalism of DFPT were made by Baroni and co-workers[3,4] and Gonze.[5–7] The developments introduced in those seminal papers showed that these responses, leading to important physical quantities, can be calculated as accurately as the DFT ground-state properties which have become so familiar in recent years. Notable examples include the calculation of macroscopic dielectric constants in semiconductors such as silicon,[8] phonon spectra,[4] Raman scattering,[9] and nuclear magnetic resonance chemical shift tensors.[10,11]

The variational formulation of DFPT due to Gonze[5] is particularly elegant. It is based upon the $2n+1$ theorem which states that the $(2n+1)$th-order response of the energy may be calculated using only the nth-order response of the Kohn-Sham orbitals. It can be deduced that even-order derivatives obey a stationary principle, or for diagonal terms a minimum principle. This allows the method to be formulated as a problem of minimization with respect to the basis-set coefficients which may be solved using efficient algorithms such as conjugate gradients. The variational formalism has the inherent advantage that it is intrinsically self-consistent and does not require a separate self-consistency cycle. Further, the computational cost is comparable to that of a single-point energy self-consistent calculation, although there are further implications when symmetry is considered.

We have implemented DFPT for lattice dynamics and electric field responses using the plane-wave pseudopotential formalism within the CASTEP code.[12,13] In this paper we will describe developments of the theory and implementation of DFPT. In particular we give the formalism to compute the first-order exchange-correlation potential in the generalized gradient approximation (GGA) for incommensurate perturbations in a fast Fourier transform–(FFT) grid consistent manner. We present an efficient all-bands preconditioned conjugate-gradient solver for the self-consistent variational minimization of the second-order energy. We discuss the use of space group symmetry to optimize the number of self-consistent calculations needed to obtain the full dynamical matrix of lattice dynamics and the implementation on a massively parallel supercomputer. Finally we will present some results of DFPT applied to lattice dynamical and dielectric

problems. We also benchmark against previous calculations (where results are available) to demonstrate the consistency of our implementation and methods.

II. FUNDAMENTALS

The theory of DFPT is discussed in detail in the review by Baroni *et al.*[4] Our implementation is based on the variational scheme of Gonze[6,7] and we use the same notation. The ground-state energy of the system is expanded in a perturbation series in the parameter λ which, for example, could be an atomic perturbation described by some wave vector $\boldsymbol{q}$, or an external field

$$E = \lambda^0 E^{(0)} + \lambda^1 E^{(1)} + \lambda^2 E^{(2)} + \cdots , \tag{1}$$

and similarly, so are the Kohn-Sham orbitals,

$$\psi^i_{\boldsymbol{k}} = \lambda^0 \psi^{(0)}_{i,\boldsymbol{k}} + \lambda^1 \psi^{(1)}_{i,\boldsymbol{k}} + \lambda^2 \psi^{(2)}_{i,\boldsymbol{k}} + \cdots , \tag{2}$$

and likewise for the density.

The diagonal elements of the dynamical matrix of lattice dynamics are given by $E^{(2)}_{\mathrm{el},-\boldsymbol{q},\boldsymbol{q}}$ which is the second-order energy given by an atomic perturbation described by an arbitrary wave vector $\boldsymbol{q}$. Our variational expression for this is modified from that given by Gonze and Lee[6] in order to describe a first-order exchange-correlation (XC) potential when the functional depends on the gradient of the density in the GGA; namely,

$$\begin{aligned} E^{(2)}_{\mathrm{el},-\boldsymbol{q},\boldsymbol{q}}\{u^{(0)};u^{(1)}\} = {} & \frac{\Omega_0}{(2\pi)^3}\int_{\mathrm{BZ}} \sum_m^{\mathrm{occ}} s[\langle u^{(1)}_{m\boldsymbol{k},\boldsymbol{q}}|H^{(0)}_{\boldsymbol{k}+\boldsymbol{q},\boldsymbol{k}+\boldsymbol{q}} - \epsilon^{(0)}_{m\boldsymbol{k}}|u^{(1)}_{m\boldsymbol{k},\boldsymbol{q}}\rangle + \langle u^{(1)}_{m\boldsymbol{k},\boldsymbol{q}}|v^{(1)}_{\mathrm{sep},\boldsymbol{k}+\boldsymbol{q},\boldsymbol{k}}|u^{(0)}_{m\boldsymbol{k}}\rangle \\ & + \langle u^{(0)}_{m\boldsymbol{k}}|v^{(1)}_{\mathrm{sep},\boldsymbol{k},\boldsymbol{k}+\boldsymbol{q}}|u^{(1)}_{m\boldsymbol{k},\boldsymbol{q}}\rangle + \langle u^{(0)}_{m\boldsymbol{k}}|v^{(2)}_{sep,\boldsymbol{k},\boldsymbol{k}}|u^{(0)}_{m\boldsymbol{k}}\rangle]d\boldsymbol{k} \\ & + \frac{1}{2}\int_{\Omega_0}\{[\bar{n}^{(1)}_{\boldsymbol{q}}(\boldsymbol{r})]^*[\bar{v}^{(1)}_{\mathrm{loc},\boldsymbol{q}}(\boldsymbol{r}) + \bar{v}^{(1)}_{\mathrm{XC0},\boldsymbol{q}}(\boldsymbol{r})] + [\bar{n}^{(1)}_{\boldsymbol{q}}(\boldsymbol{r})][\bar{v}^{(1)}_{\mathrm{loc},\boldsymbol{q}}(\boldsymbol{r}) + \bar{v}^{(1)}_{\mathrm{XC0},\boldsymbol{q}}(\boldsymbol{r})]^*\}d\boldsymbol{r} \\ & + \frac{1}{2}\int_{\Omega_0}[\bar{v}^{(1)}_{\mathrm{XC},\boldsymbol{q}}(\boldsymbol{r}) + \bar{v}^{(1)}_{\mathrm{H},\boldsymbol{q}}(\boldsymbol{r})]^*\bar{n}^{(1)}_{\boldsymbol{q}}(\boldsymbol{r})d\boldsymbol{r} + \int_{\Omega_0} n^{(0)}(\boldsymbol{r})\bar{v}^{(2)}_{\mathrm{loc}}(\boldsymbol{r})d\boldsymbol{r} + \frac{1}{2}\left.\frac{d^2E_{\mathrm{H\,XC}}}{d\lambda\, d\lambda^*}\right|_{n^{(0)}}, \end{aligned} \tag{3}$$

where the symbols are defined in Ref. 6. A numeric superscript (n) denotes the nth-order response of the corresponding ground-state quantity. Alternatively superscripts ε_α and $\tau_{\kappa,\alpha}$ denote first-order electric field and atomic displacement perturbed quantities of Cartesian direction α and atom number κ. The overbar in the first-order charge densities and potentials denotes that each is a complex, phase-factorized cell-periodic quantity which may be stored on the usual FFT grid for the primitive cell. The first-order charge density is given by the expression

$$\bar{n}^{(1)}(\boldsymbol{r}) = \frac{2}{(2\pi)^3}\int_{\mathrm{BZ}} \sum_m^{\mathrm{occ}} s u^{(0)^*}_{m\boldsymbol{k}}(\boldsymbol{r}) u^{(1)}_{m\boldsymbol{k},\boldsymbol{q}}(\boldsymbol{r})d\boldsymbol{k}. \tag{4}$$

Equation (3) is valid in the case of GGA XC functionals, which Eq. (15) of Ref. 7 is not. $E^{(2)}_{\mathrm{el},-\boldsymbol{q},\boldsymbol{q}}\{u^{(0)};u^{(1)}\}$ is minimized with respect to the first-order response orbitals under the orthogonality constraint

$$\langle u^{(0)}_{m\boldsymbol{k}+\boldsymbol{q}}|u^{(1)}_{n\boldsymbol{k},\boldsymbol{q}}\rangle = 0 \tag{5}$$

in the parallel transport gauge.

In our implementation, we use a real-space integration to evaluate the Hartree contribution. Though this might appear less efficient than the reciprocal-space sum of Ref. 7 the energy is most efficiently computed by summing all the first-order potentials

$$\bar{v}^{(1)}_{\mathrm{tot},\boldsymbol{q}}(\boldsymbol{r}) = \bar{v}^{(1)}_{\mathrm{XC},\boldsymbol{q}}(\boldsymbol{r}) + \bar{v}^{(1)}_{\mathrm{H},\boldsymbol{q}}(\boldsymbol{r}) + \bar{v}^{(1)}_{\mathrm{loc},\boldsymbol{q}}(\boldsymbol{r}) \tag{6}$$

whereupon only a single integral of a first-order local potential multiplied by a density is required in the evaluation of Eq. (3).

A similar modification yields the expression for the second-order energy with respect to electric field perturbations also valid for GGA functionals,

$$\begin{aligned} E^{*\varepsilon_\alpha\varepsilon_\alpha}_{\mathrm{el}}[u^{(0)};u^{\varepsilon_\alpha}] = {} & \frac{\Omega_0}{(2\pi)^3}\int_{\mathrm{BZ}} \sum_m^{\mathrm{occ}} s[\langle u^{\varepsilon_\alpha}_{m\boldsymbol{k}}|H^{(0)}_{\boldsymbol{k},\boldsymbol{k}} - \epsilon^{(0)}_{m\boldsymbol{k}}|u^{\varepsilon_\alpha}_{m\boldsymbol{k}}\rangle \\ & + \langle u^{\varepsilon_\alpha}_{m\boldsymbol{k}}|iu^{k_\alpha}_{m\boldsymbol{k}}\rangle + \langle iu^{k_\alpha}_{m\boldsymbol{k}}|u^{\varepsilon_\alpha}_{m\boldsymbol{k}}\rangle]d\boldsymbol{k} \\ & + \frac{1}{2}\int_{\Omega_0}[v^{\varepsilon_\alpha}_{\mathrm{XC}}(\boldsymbol{r}) + v^{\varepsilon_\alpha}_{\mathrm{H},\boldsymbol{q}}(\boldsymbol{r})]^* n^{\varepsilon_\alpha}(\boldsymbol{r})d\boldsymbol{r}. \end{aligned} \tag{7}$$

Evaluation of the second-order energies due to either an atomic position or electric field perturbation is the first step in obtaining phonon frequencies or bulk polarizabilities. These expressions give the diagonal terms of a dynamical matrix or polarizability tensor. Though the nonvariational expressions for off-diagonal terms are simple in principle, in practice the different symmetries of the perturbations and consequently different irreducible wedges complicates the Brillouin-zone integration. This will be discussed in Sec. VI.

The mixing of two perturbations is not constrained to two perturbations of the same type. For example the Born effective charges may be obtained by a mixed atomic displacement and electric field perturbation.

III. FIRST-ORDER XC POTENTIAL IN THE GGA

The treatment of the exchange-correlation term is relatively straightforward in the case of the local density approximation (LDA), but more complicated for the GGAs. Here we describe a general method for incorporating a GGA within the linear response formalism.

Equations (3) and (7) and their corresponding gradients require the evaluation of the first-order exchange-correlation potential,

$$\bar{v}^{(1)}_{\mathrm{XC},\boldsymbol{q}}(\boldsymbol{r}) = \int \left.\frac{\delta^2 \varepsilon_{\mathrm{XC}}}{\delta n(\boldsymbol{r})\,\delta n(\boldsymbol{r}')}\right|_{n^{(0)}(\boldsymbol{r})} e^{-i\boldsymbol{q}\cdot(\boldsymbol{r}-\boldsymbol{r}')}\bar{n}^{(1)}_{\boldsymbol{q}}(\boldsymbol{r}')d\boldsymbol{r}', \quad (8)$$

where the quantities with overbars are, as usual, phase factorized and cell periodic. In the case of the LDA this simplifies to

$$\bar{v}^{(1)}_{\mathrm{XC;LDA}}(\boldsymbol{r}) = \left.\frac{dv_{\mathrm{XC}}}{dn}\right|_{n^{(0)}(\boldsymbol{r})} \bar{n}^{(1)}_{\boldsymbol{q}}(\boldsymbol{r}),$$

where the derivative is straightforward to evaluate analytically. However, the second functional derivative of GGA functionals is nondiagonal and the integral in Eq. (8) does not disappear. Putrino *et al.*[10] pointed out that evaluating the second functional derivative was both analytically cumbersome and numerically unstable. They suggested that $v^{(1)}_{\mathrm{XC}}$ could be calculated using a finite-difference derivative of the XC potential, but that method is not applicable to incommensurate perturbations where $v^{(1)}_{\mathrm{XC}}$ is not simply the derivative of v_{XC} with respect to the perturbation.

Favot and Dal Corso[14] presented a formula where $v^{(1)}_{\mathrm{XC}}$ is given not as the analytical functional derivative of the GGA formula but as a FFT grid-consistent derivative at finite cutoff. However, they did not show how to treat incommensurate perturbations. A very similar formula was presented by Egli and Billeter.[15]

Our method for calculating $\bar{v}^{(1)}_{\mathrm{XC},\boldsymbol{q}}(\boldsymbol{r})$ begins from the work of White and Bird[16] who noted that the true analytic exchange-correlation potential has Fourier components of too high spatial frequency to be representable on the usual FFT grid of a plane-wave basis set. They introduced an approximate XC potential defined only on grid points $\boldsymbol{R}$,

$$v_{\mathrm{XC}}(\boldsymbol{R}) = \frac{\partial f_{\mathrm{XC}}}{\partial n(\boldsymbol{R})} + \sum_{\boldsymbol{R}'} \frac{\partial f_{\mathrm{XC}}}{\partial \nabla n(\boldsymbol{R}')} \cdot \frac{d\nabla n(\boldsymbol{R}')}{dn(\boldsymbol{R})} \quad (9)$$

where $f_{\mathrm{XC}}(n,\nabla n)$ is the particular GGA kernel. For notational convenience we define

$$f_{nn} = \frac{\partial^2 f_{\mathrm{XC}}}{\partial n(\boldsymbol{R})\partial n(\boldsymbol{R})}, \quad f_{ng} = \frac{\partial^2 f_{\mathrm{XC}}}{\partial n(\boldsymbol{R})\partial \nabla n(\boldsymbol{R})},$$

$$f_{gn} = \frac{\partial^2 f_{\mathrm{XC}}}{\partial \nabla n(\boldsymbol{R})\partial n(\boldsymbol{R})}, \quad f_{gg} = \frac{\partial^2 f_{\mathrm{XC}}}{\partial \nabla n(\boldsymbol{R})\partial \nabla n(\boldsymbol{R})}, \quad (10)$$

and corresponding quantities f'_{nn}, f'_{ng}, f'_{gn}, and f'_{gg} which are evaluated at $\boldsymbol{R}'$ instead of $\boldsymbol{R}$.

Taking a variation of Eq. (9) with respect to $n(\boldsymbol{R})$ and $\nabla n(\boldsymbol{R})$, treating them as independent variables, and noting that $\delta\nabla n(\boldsymbol{R}) = \nabla \delta n(\boldsymbol{R})$ for a periodic density $n(\boldsymbol{R})$ yields

$$\begin{aligned}
\delta v_{\mathrm{XC}} &= f_{nn}\delta n(\boldsymbol{R}) + f_{gn}\cdot\delta\nabla n(\boldsymbol{R}) + \sum_{\boldsymbol{R}'}\left(f'_{ng}\cdot\frac{d\nabla n(\boldsymbol{R}')}{dn(\boldsymbol{R})}\delta n(\boldsymbol{R}') + f'_{gg}\cdot\frac{d\nabla n(\boldsymbol{R}')}{dn(\boldsymbol{R})}\cdot\delta\nabla n(\boldsymbol{R}')\right)\\
&= f_{nn}\delta n(\boldsymbol{R}) + f_{gn}\cdot\delta\nabla n(\boldsymbol{R}) - \frac{1}{N}\sum_{\boldsymbol{R}'}\sum_{\boldsymbol{G}} i\boldsymbol{G}e^{i\boldsymbol{G}(\boldsymbol{R}-\boldsymbol{R}')}[f'_{ng}\delta n(\boldsymbol{R}') + f'_{gg}\delta\nabla n(\boldsymbol{R}')]\\
&= f_{nn}\delta n(\boldsymbol{R}) + f_{gn}\cdot\delta\nabla n(\boldsymbol{R}) - \nabla\cdot[f'_{ng}\delta n(\boldsymbol{R}) + f'_{gg}\cdot\delta\nabla n(\boldsymbol{R})], \quad (11)
\end{aligned}$$

where both steps use the identity that on the periodic grid

$$\nabla n(\boldsymbol{R}) = \frac{1}{N}\sum_{\boldsymbol{G}}\sum_{\boldsymbol{R}'} i\boldsymbol{G}n(\boldsymbol{R}')e^{i\boldsymbol{G}\cdot(\boldsymbol{R}'-\boldsymbol{R})}. \quad (12)$$

We identify $\delta n(\boldsymbol{R})$ above with $n^{(1)}(\boldsymbol{r})$ in the DFPT formalism and δv_{XC} with $v^{(1)}(\boldsymbol{r})$, which are incommensurate with the primitive cell. To represent densities and potentials on the periodic FFT grid we work with the complex, periodic (i.e., Bloch-function-like) quantities $\bar{n}^{(1)}(\boldsymbol{R})$ and $\bar{v}^{(1)}(\boldsymbol{R})$ given by,

$$n^{(1)}(\boldsymbol{R}) = \exp(i\boldsymbol{q}\cdot\boldsymbol{R})\bar{n}^{(1)}(\boldsymbol{R}). \quad (13)$$

Applying the chain rule to Eq. (13) gives

$$\nabla n^{(1)}(\boldsymbol{R}) = \exp(i\boldsymbol{q}\cdot\boldsymbol{R})[i\boldsymbol{q}\bar{n}^{(1)}(\boldsymbol{R}) + \nabla\bar{n}^{(1)}(\boldsymbol{R})]. \quad (14)$$

Substituting Eqs. (13) and (14) into Eq. (11) and expanding the contents of the square brackets gives

$$\begin{aligned}
v^{(1)}(\boldsymbol{R}) = \exp(i\boldsymbol{q}\cdot\boldsymbol{R})&[f_{nn}\bar{n}^{(1)}(\boldsymbol{R}) + i\boldsymbol{q}\cdot f_{gn}\bar{n}^{(1)}(\boldsymbol{R})\\
&+ f_{gn}\cdot\nabla\bar{n}^{(1)}(\boldsymbol{R})] - \exp(i\boldsymbol{q}\cdot\boldsymbol{R})\\
&\times(i\boldsymbol{q}+\nabla)\cdot[f_{ng}\bar{n}^{(1)}(\boldsymbol{R}) + i\boldsymbol{q}f_{gg}\bar{n}^{(1)}(\boldsymbol{R})\\
&+ f_{gg}\nabla\bar{n}^{(1)}(\boldsymbol{R})]. \quad (15)
\end{aligned}$$

Defining $\bar{v}^{(1)}(\boldsymbol{R})$ by $v^{(1)}(\boldsymbol{R})=\exp(i\boldsymbol{q}\cdot\boldsymbol{R})\bar{v}^{(1)}(\boldsymbol{R})$ the incommensurate phase factor is eliminated to yield

$$\bar{v}^{(1)}(\boldsymbol{R}) = [f_{nn}\bar{n}^{(1)}(\boldsymbol{R}) + f_{gn}\cdot(i\boldsymbol{q}+\nabla)\bar{n}^{(1)}(\boldsymbol{R})] - (i\boldsymbol{q}+\nabla)\cdot[f_{ng}\bar{n}^{(1)}(\boldsymbol{R}) + f_{gg}\cdot(i\boldsymbol{q}+\nabla)\bar{n}^{(1)}(\boldsymbol{R})], \tag{16}$$

where all density and potential terms are cell periodic, commensurate, complex quantities, which have a straightforward representation on the computational FFT grid.

The desired XC potential $\bar{v}^{(1)}(\boldsymbol{R})$ may be evaluated on the FFT grid by first computing $\nabla\bar{n}^{(1)}(\boldsymbol{R})$ (four FFTs) and then applying Eq. (16) (another four FFTs). Equation (10) require the derivatives of the GGA kernel $f_{\mathrm{XC}}(n,|\nabla n(\boldsymbol{R})|)$ with respect to $\nabla n(\boldsymbol{R})$. These are re-expressed as

$$f_{gn} = \frac{\nabla n(\boldsymbol{R})}{|\nabla n(\boldsymbol{R})|}\frac{\partial f_{\mathrm{XC}}}{\partial|\nabla n(\boldsymbol{R})|\partial n(\boldsymbol{R})}, \tag{17}$$

$$f_{gg} = \left(\frac{1}{|\nabla n(\boldsymbol{R})|} - \frac{\nabla n(\boldsymbol{R})\,\nabla\, n(\boldsymbol{R})}{|\nabla n(\boldsymbol{R})|^3}\right)\frac{\partial f_{\mathrm{XC}}}{\partial|\nabla n(\boldsymbol{R})|} + \frac{\nabla n(\boldsymbol{R})\,\nabla\, n(\boldsymbol{R})}{|\nabla n(\boldsymbol{R})|^2}\frac{\partial f_{\mathrm{XC}}}{\partial|\nabla n(\boldsymbol{R})|\partial|\nabla n(\boldsymbol{R})|}, \tag{18}$$

where the last expression is interpreted as a tensor dyad product. The derivatives of f_{XC} on the right-hand side of the above expressions are easily evaluated either analytically[15] or numerically. We use a central-difference numerical differentiation of the chosen GGA kernel. Thus we can evaluate the first-order XC potential at an incommensurate wave vector while representing all quantities as Bloch-factorized, periodic functions which can be mapped onto the computational FFT grid.

IV. COMPUTATIONAL METHODS

A. All-bands conjugate-gradient solver

The central problem is to find a set of first-order orbitals which minimize the second-order energies of Eqs. (3) and (7) subject to the orthogonality condition. The prerequisite is a set of zeroth-order orbitals $u^{(0)}_{m\boldsymbol{k}}$ and $u^{(0)}_{m\boldsymbol{k}+\boldsymbol{q}}$. For an incommensurate perturbation with wave vector $\boldsymbol{q}$ the zeroth-order orbitals at $\boldsymbol{k}+\boldsymbol{q}$ are required. The approach of Gonze[6,7] is to make use of the orbitals computed during the ground-state self-consistent procedure which are available on the Monkhorst-Pack grid. This limits the choice of phonon wave vector $\boldsymbol{q}$ to the difference between any pair of the Monkhorst-Pack $\boldsymbol{k}$ points. We use a more general approach which is to compute a set of $u^{(0)}_{m\boldsymbol{k}+\boldsymbol{q}}$ using a non-self-consistent band structure calculation in the self-consistent Kohn-Sham potential of the ground state. With this approach, any $\boldsymbol{q}$ vector is allowed. Further to this, we make use of the point group symmetry of the orbitals to reduce the computational cost which we describe in detail, below.

We obtain the first-order orbitals using a preconditioned conjugate-gradient minimizer. Our method varies the coefficients of all bands simultaneously using a method similar to a ground-state search.[17] This method uses more memory than a band-by-band approach to store the gradients; however, the computational time is considerably lower because only one evaluation of the first-order density and potentials is required per conjugate-gradient cycle. Construction of the first-order density is an expensive operation involving many applications of a fast Fourier transform. In a band-by-band approach the computation of the first-order density may be optimized by incremental updates for each band but the nonlinear first-order XC potential cannot.

We obtain a total gradient vector from Eq. (3) of the form

$$\zeta^i_{m,\boldsymbol{k}} = -P_c[(H^{(0)}-\epsilon_{m,\boldsymbol{k}})|u^{(1)}_{m\boldsymbol{k}}\rangle + H^{(1)}|u^{(0)}_{m\boldsymbol{k}}\rangle], \tag{19}$$

where $H^{(1)}$ is the total self-consistent first-order perturbation Hamiltonian, P_c is the projection orthogonal to the occupied states, and i is an iteration count. This is a vector in the product space of basis-set coefficients ($\boldsymbol{G}$ vector), bands m, and $\boldsymbol{k}$ points in the irreducible BZ. The preconditioning matrix multiplies this total gradient

$$\eta^i = P_c K\zeta^i \tag{20}$$

and the conjugate direction is formed as

$$\phi^i_{m,\boldsymbol{k}} = \eta^i_{m,\boldsymbol{k}} + \gamma^i\phi^{i-1}_{m,\boldsymbol{k}}, \tag{21}$$

where γ^i is given by the Fletcher-Reeves formula[18]

$$\gamma^i = \frac{\sum_{m,\boldsymbol{k}}\langle\eta^i_{m,\boldsymbol{k}}|\phi^i_{m,\boldsymbol{k}}\rangle}{\sum_{m,\boldsymbol{k}}\langle\eta^{i-1}_{m,\boldsymbol{k}}|\phi^{i-1}_{m,\boldsymbol{k}}\rangle}. \tag{22}$$

The second-order energy is minimized along this direction using a quadratic line minimizer. The step size is determined using the initial gradient and value of the energy and a second evaluation of the energy at a trial point. A full line search is unnecessary because Eq. (3) is a quadratic form in the presence of the orthogonality constraints. To obtain an accurate location of the quadratic minimum in a single step requires that the trial step is of similar numerical magnitude to the final step. Our method chooses an initial guess for the trial step based on the previous iteration and scales it if necessary.

Within the spirit of this all-bands approach, we precompute and store the nonlocal terms

$$v^{(1)}_{\mathrm{sep},\boldsymbol{k}+\boldsymbol{q},\boldsymbol{k}}|u^{(0)}_{m\boldsymbol{k}}\rangle \tag{23}$$

outside the iterative procedure, thus further increasing the speed of the minimizer. We find that storage of this quantity saves approximately 20% of the CPU time.

We investigated a number of different preconditioning algorithms: that of Teter *et al.*[19] (TPA), the modification due to Kresse and Furthmüller[20] (RTPA), and one due to Putrino *et al.*[10] (PSP) that was specifically designed for use in DFPT applications.

An example of the convergence rate of the second-order energy for an atomic position perturbation minimized with these preconditioners is shown in Fig. 1. First, by comparing Figs. 1(a) and 1(b), it can be seen that a conjugate-gradient algorithm converges approximately twice as fast as a simpler

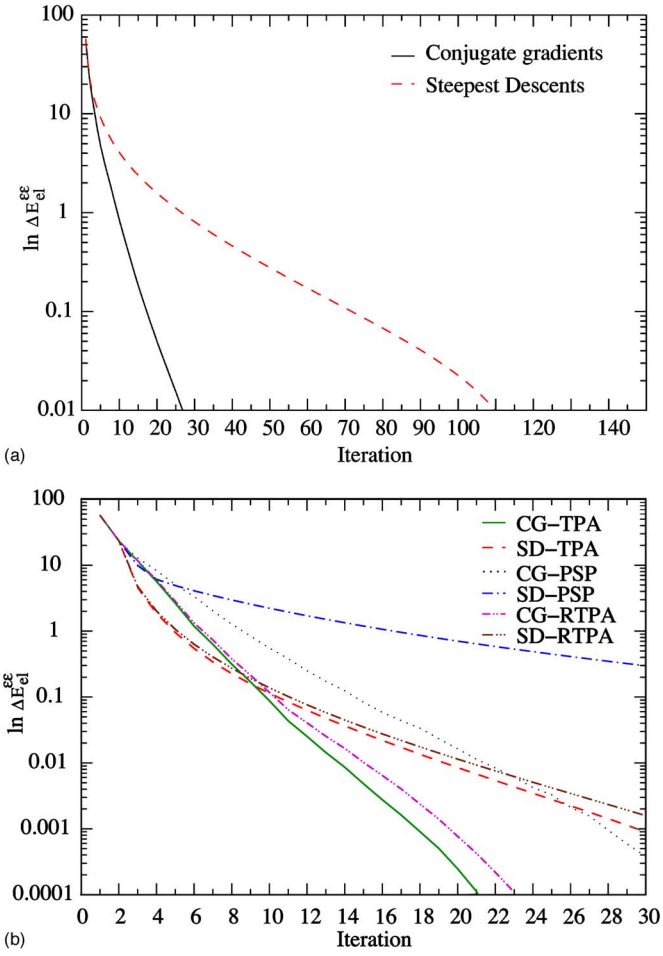

FIG. 1. (Color online) (a) The second-order energy as a function of iteration number (scaled to show equivalent computational effort) for the steepest-decent (SD) and conjugate-gradient (CG) methods. (b) The effect of various preconditioning schemes for both CD and SD methods. Note the change in the x axis from (a).

steepest-descent method. An iteration is defined as a minimization in a single search direction so that each iteration takes a comparable amount of time. In both cases the TPA and RTPA preconditioners converge the second-order energy at approximately the same rate. The best performing preconditioner was the original TPA variant, despite being intended for a ground-state DFT search, and the PSP preconditioner showed the worst performance despite being specifically designed for DFPT calculations. However, the differences between each are relatively small. Though inclusion of a preconditioner is obviously advantageous, the choice of which variant should be a secondary consideration after use of conjugate gradients versus steepest descents.

V. DYNAMICAL MATRIX SYMMETRY

The central task in any lattice dynamics calculation is the construction of the dynamical matrix. In the absence of symmetry (other than the Hermitian character of the dynamical matrix) this requires $3N$ perturbations and variational minimization using Eq. (3) and $(9N^2-3N)/2$ mixed perturbation calculations if there are N atoms in the unit cell. This number may be reduced by a large factor by exploiting the symmetry equivalence between elements of the dynamical matrix consequent on the space group symmetry of the crystal and the phonon wave vector $\boldsymbol{q}$. For example, in the diamond structure containing two identical atoms per cell, only one variational minimization is needed instead of 6 at $\boldsymbol{q}=\boldsymbol{0}$.

The theory of the application of symmetry to lattice dynamics was set out by Maradudin and Vosko[21] and Warren[22] using the irreducible multiplier representations of the space group. The dynamical matrix $D_{\alpha\alpha'}^{\kappa\kappa'}(\boldsymbol{q})$ is a $3N\times 3N$ matrix where the indices κ and κ' refer to atoms and α and α' refer to Cartesian directions and $\boldsymbol{q}$ is the phonon wave vector. They showed that if $\boldsymbol{q}$ is invariant under the operation of a space group symmetry operation $\{\boldsymbol{S}|\boldsymbol{v}_S\}$ with rotation matrix $\boldsymbol{S}$ and translation vector $\boldsymbol{v}_S$ then the dynamical matrix transforms as

$$D_{\alpha\alpha'}^{\kappa\kappa'}(\boldsymbol{q}) = \boldsymbol{T}^{-1}(\boldsymbol{q};\boldsymbol{S})D_{\alpha\alpha'}^{\kappa\kappa'}(\boldsymbol{q})\boldsymbol{T}(\boldsymbol{q};\boldsymbol{S}), \tag{24}$$

where

$$\boldsymbol{T}(\boldsymbol{q};\boldsymbol{S}) = S_{\alpha\beta}\delta(\kappa,F_0(\kappa';S))\exp[i\boldsymbol{q}\cdot(\boldsymbol{x}_\kappa-\boldsymbol{S}\boldsymbol{x}_{\kappa'})] \tag{25}$$

is a matrix from the irreducible multiplier representation of the group of $\boldsymbol{q}$. Here $F_0(\kappa';S)$ is the index of the atom related to atom κ' by the symmetry operation $\{\boldsymbol{S}|\boldsymbol{v}_S\}$, $\boldsymbol{x}_\kappa$ is the coordinates of atom κ, and δ is the usual Kronecker delta symbol. If one of the space group operations carries $\boldsymbol{q}\rightarrow-\boldsymbol{q}$ (including but not limited to the case of an inversion) then the time-reversal symmetry gives rise to additional invariances (detailed in Ref. 21).

From a computational perspective the problem is to determine a minimal subset of the elements of $D_{\alpha\alpha'}^{\kappa\kappa'}(\boldsymbol{q})$ and the relationships between elements needed to construct the complete matrix. Our approach is similar to that of Worlton and Warren.[23] A matrix D_{rand} of the same dimensions as $D_{\alpha\alpha'}^{\kappa\kappa'}(\boldsymbol{q})$ is constructed to be maximally random while satisfying all of the invariances of the form of Eq. (24) and also Hermitian. This is accomplished by the following algorithm. A Hermitian matrix $D_{\text{rand}}^{\text{init}}$ is constructed using a pseudo-random-number generator, and D_{rand} is generated by the formula

$$D_{\text{rand}} = \sum_{j=1}^{g(\boldsymbol{q})} \boldsymbol{T}^{-1}(\boldsymbol{q};\boldsymbol{S})D_{\text{rand}}^{\text{init}}\boldsymbol{T}(\boldsymbol{q};\boldsymbol{S}) \tag{26}$$

from which it is straightforward to demonstrate[23] that D_{rand} satisfies Eq. (24) for all operations in the space group. A very similar procedure is subsequently applied to make D_{rand} also satisfy the time-reversal invariances.

The D_{rand} generated by this procedure thus satisfies all of the symmetries of the crystal but is otherwise random. The desired relationships among elements of $D_{\alpha\alpha'}^{\kappa\kappa'}(\boldsymbol{q})$ are determined from an analysis of those of D_{rand}. These may take the form of elements equal to zero, elements that are equal in magnitude and complex phase, elements that are equal in magnitude but of opposite phase, and elements that are equal in magnitude but rotated or counter-rotated in phase. These conditions are satisfied to a high degree of numerical preci-

sion and are easily identifiable from the values of D_{rand}. To be sure that a value of zero is not produced accidentally, the initial random elements of $D_{\text{rand}}^{\text{init}}$ are biased away from zero.

A further consequence of the symmetry is to fix the phases of some elements of the dynamical matrix, to either an absolute or a $\boldsymbol{q}$-dependent value. Our analysis goes further than that of Worlton and Warren[23] in detecting symmetry-determined phases and relative phases of elements. This is achieved by repeating the analysis with a new initial $D_{\text{rand}}^{\text{init}}$ generated using an independent sequence of pseudo-random-numbers. Those phases and phase relationships that are in common are marked as being symmetry determined.

In addition to the symmetry relationships so far discussed, it is possible in some structures with hexagonal and trigonal space groups for linear relationships to exist among three or more elements. The linear symmetry analysis is unable to detect these relationships, and in such cases more than the irreducible minimum of variational DFPT calculations will be performed.

During the calculation of $D_{\alpha\alpha'}^{\kappa\kappa'}(\boldsymbol{q})$ the symmetry information is used as follows. Elements that are zero by symmetry are not calculated. On every calculation of a dynamical matrix element of a given a value, all elements which have equal magnitude by symmetry are also set to the same value. The symmetry-determined phase information is used to set the phases of the related elements. After an element has been assigned to, it is marked as "already computed" and subsequent iterations of the atom or direction loops omit any calculations if this flag is set for a particular element.

A very similar analysis is performed to establish the symmetries of the set of Born effective charge tensors. These resemble those of the leading 3×3 block diagonal of the dynamical matrix with the difference that there is no requirement for matrix symmetry.

Finally the symmetry of the dielectric permittivity (and polarizability) is that of a symmetric tensor. A simplified version of the algorithm used for the dynamical matrix is used to avoid unnecessary recomputation.

VI. SYMMETRY AND BRILLOUIN-ZONE SAMPLING

Space group symmetry also plays an important role in the sampling of the electronic BZ for sums such as those in Eq. (3) and the first-order electron density $n_{\boldsymbol{q}}^{(1)}(\boldsymbol{r})$ constructed according to

$$n_{\boldsymbol{q}}^{(1)}(\boldsymbol{r}) = \sum_{S=1}^{N_S} S \sum_{\boldsymbol{k}=1}^{N_{\boldsymbol{k}}} w_{\boldsymbol{k}} \sum_{m}^{\text{occ}} u_{m\boldsymbol{k}}^{(0)*}(\boldsymbol{r}) u_{m\boldsymbol{k}}^{(1)}(\boldsymbol{r}), \tag{27}$$

where N_S is the number of symmetry operations, $N_{\boldsymbol{k}}$ is the number of $\boldsymbol{k}$ points in the irreducible set, $w_{\boldsymbol{k}}$ is weight applied to $\boldsymbol{k}$ and m indexes the occupied bands. The set of $\boldsymbol{k}$ points is usually derived from a Monkhorst-Pack grid[24] and folded to a symmetry irreducible set under the operations of the group $\{S\}$, the subgroup of the space group under which the perturbation is invariant. In the case of an atomic displacement perturbation this is the group of $\boldsymbol{q}$ and α, which is smaller than the full space group. The irreducible set of $\boldsymbol{k}$ points $\{\boldsymbol{k}\}$ and weights $\{w_{\boldsymbol{k}}\}$ is in general larger than for the self-consistent-field calculation. In particular expression (3) in not invariant under time-reversal symmetry and the set must include both $\boldsymbol{k}$ and $-\boldsymbol{k}$ unless $2\boldsymbol{q}$ is zero or a reciprocal lattice vector.

As mentioned in Sec. IV A, the $\{u_{m\boldsymbol{k}}^{(0)}\}$ are constructed using a non-self-consistent "band structure" calculation using the self-consistent ground-state density and potential. It is possible to economize on the number of these calculations by using the symmetry relations among the set which arise because of the higher symmetry of the unperturbed space group. In reciprocal space the wave function coefficients transform under $\{\boldsymbol{S}|\boldsymbol{v}_S\}$ as

$$c_{m\boldsymbol{S}\boldsymbol{k}}(\boldsymbol{S}\boldsymbol{G}) = \exp[-2\pi i \boldsymbol{S}\cdot(\boldsymbol{k}+\boldsymbol{G})\cdot\boldsymbol{v}_S] c_{m\boldsymbol{k}}(\boldsymbol{G}). \tag{28}$$

This is straightforward to implement if the FFT grid is mapped onto a three-dimensional array as it is in the serial or $\boldsymbol{k}$ point parallel case. When the grid is distributed across processors for $\boldsymbol{G}$-vector parallelism, then interprocessor communication is required since the coefficients on the left and right hand sides of Eq. (28) in general reside on different processors. In that case the grid is reconstructed by gathering coefficients onto the master node, transforming according to Eq. (28), and scattering to the new locations. This is done one band at a time to limit the additional storage of a full grid on a single processor.

While the above procedure suffices for terms diagonal in the perturbation, off-diagonal terms in the dynamical matrix and dielectric permittivity tensor must be evaluated using a "mixed-perturbation" formula such as Eq. (16) or (38) in Ref. 7. This involves the first-order orbitals with respect to just one of the perturbations which have been evaluated on a $\boldsymbol{k}$ point set irreducible with respect to its symmetry. The other perturbation does not in general have the same symmetry, and so the Brillouin-zone integral cannot be evaluated using the same weighted sum as used to obtain the first-order orbitals. Using Eq. (28) it is straightforward to show that

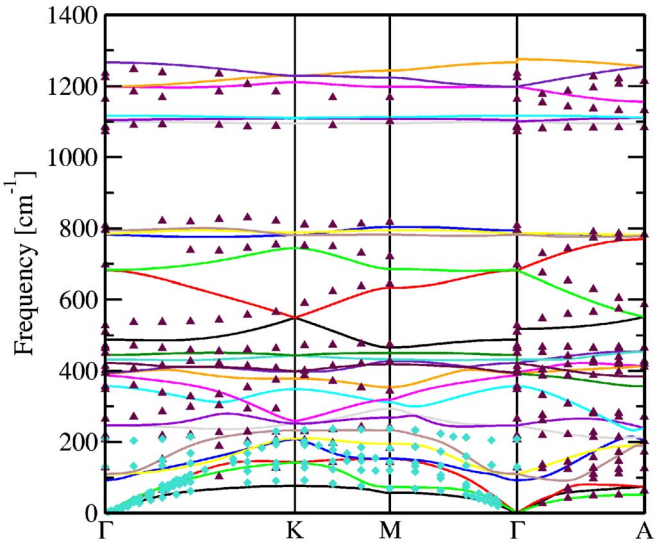

FIG. 2. (Color online) The phonon dispersion curve for α-quartz is shown along several lines of high symmetry. Experimental results are shown by solid symbols.

TABLE I. Zone-center vibrational frequencies of α-quartz (in cm^{-1}) compared with previous calculations and experiment. Previous plane-wave (PW) and all-electron (AE) results are from Refs. 35 and 36, respectively. Experimental results are extrapolated to the athermal limit as cited in results.

Mode	PW LDA[a]	AE LDA[b]	PW LDA[c]	AE PBE[b]	PW GGA[c]	Expt.[d]
*A*1	238.9	261.6	216.5	220.8	91.7	219.0
	339.3	332.3	331.4	332.0	356.5	358.0
	461.7	482.1	446.6	451.8	432.2	469.0
	1061.2	1089.1	1102.5	1050.3	1116.1	1082.0
*A*2 (TO)	341.4	326.3	336.2	326.3	387.5	361.3
	493.4	504.6	474.3	481.6	444.9	499.0
	762.4	791.1	780.2	764.6	783.1	778.0
	1056.5	1086.4	1097.5	1038.5	1103.7	1072.0
*A*2 (LO)	365.7	351.3	360.0	350.2	398.8	385.0
	540.5	543.9	523.3	528.9	518.5	553.0
	784.7	816.8	796.1	778.2	784.8	791.0
	1218.3	1249.6	1256.4	1210.4	1274.5	1230.0
E (TO)	133.3	143.4	125.1	128.8	110.0	133.0
	261.3	263.5	250.5	252.8	264.4	269.0
	377.6	376.9	369.5	372.4	392.2	393.5
	443.8	443.8	426.1	424.0	421.4	452.5
	690.8	721.7	696.1	681.5	679.6	698.0
	791.7	835.0	801.0	797.0	780.9	799.0
	1045.0	1070.3	1087.2	1030.8	1100.1	1066.0
	1128.1	1141.7	1159.8	1117.9	1198.9	1158.0
E (LO)	133.4	143.7	125.1	128.8	110.1	133.0
	263.2	266.9	252.1	255.4	246.6	269.0
	389.2	389.1	379.2	380.4	395.3	402.0
	498.6	497.2	481.7	479.8	487.1	512.0
	694.5	726.5	699.1	685.2	679.9	701.0
	803.9	844.7	811.6	806.2	792.6	811.5
	1209.5	1234.7	1245.9	1201.4	1266.2	1227.0
	1123.9	1137.3	1156.8	1115.4	1198.4	1155.0

[a]Reference 35.
[b]Reference 36.
[c]This work.
[d]Corrected values from Ref. 35.

$$\sum_{\boldsymbol{k}=1}^{\text{full BZ}} \langle u^{(0)}_{m\boldsymbol{k}} | v^{\tau_\kappa \beta} | u^{\tau_\alpha}_{m\boldsymbol{k}\boldsymbol{q}} \rangle = \frac{1}{N_S} \sum_{S=1}^{N_S} \sum_{\boldsymbol{k}=\boldsymbol{1}}^{N_{\boldsymbol{k}}} w_{\boldsymbol{k}} \exp(-2\pi i \boldsymbol{q} \cdot \boldsymbol{v}_S) \langle u^{(0)}_{m\boldsymbol{k}} | v^{\tau_\kappa S \beta} | u^{\tau_\alpha}_{m\boldsymbol{k}\boldsymbol{q}} \rangle, \tag{29}$$

where the sum on the right hand side is over the same irreducible set used for the diagonal term and where the $u^{\tau_\alpha}_{m\boldsymbol{k}\boldsymbol{q}}$ are already available. Similar formulas hold for the other terms including the nonvariational contribution to the dynamical matrix and the off-diagonal terms of the dielectric permittivity tensor.

The different symmetry and set of electronic $\boldsymbol{k}$ points in the irreducible BZ means that some flexibility is required to optimize the performance when executing on a massively parallel supercomputer. Our implementation is able to dynamically choose an optimum strategy to distribute both $\boldsymbol{k}$ points and $\boldsymbol{G}$-vector components of the FFT grid for each perturbation. This enables efficient use of very large numbers of processors with good load balancing. Alternative schemes which distribute perturbations or $\boldsymbol{q}$ points among processors have the disadvantage that the computation time varies considerably due to the different numbers of $\boldsymbol{k}$ points in the irreducible BZ, making good load balancing hard to achieve.

VII. APPLICATIONS

A. Introduction

Applications of DFPT have been presented in abundance elsewhere showing that it has become a highly successful

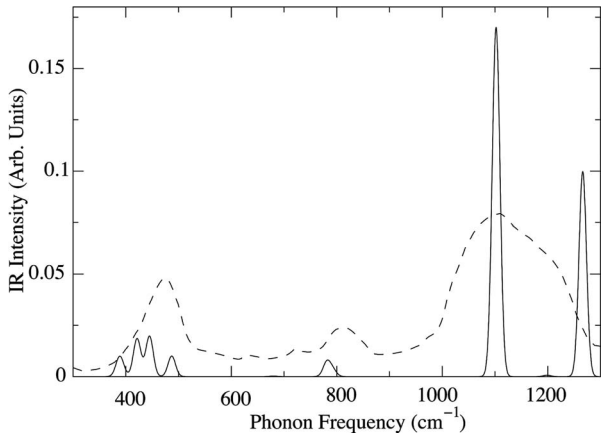

FIG. 3. The calculated ir absorption spectrum for α-quartz is shown (solid line) along with experimental results (dashed line) (Ref. 37).

addition to the density-functional total-energy toolbox. In this section, we describe a selection of results using the CASTEP DFPT code. First we demonstrate some results for α-quartz to show reliability, but also to illustrate the methods described above, such as the directional dependence as $\boldsymbol{q} \rightarrow \mathbf{0}$ of the nonanalytic behavior of phonon frequencies. Second we explain the results of some DFPT calculations for the ionic crystal $NaHF_2$ which contains some surprising and nonintuitive results, such as an effective charge of $+2e$ for a H ion. We also use this example to demonstrate that the choice of XC functional is crucial in determining the dynamical properties of such a hydrogen-bonded material. Finally we demonstrate the application to the polarizability tensor of an important molecular system, the prototypical liquid-crystal-forming molecule 5CB (4-4-pentyl-cyanobiphenyl). Further applications of CASTEP DFPT may be found in Refs. 25–27.

B. α-quartz

The low-temperature (α) phase of quartz is one of the more complex crystals for which high-quality experimental dispersion curves are available. Its dielectric permittivity and Born effective charges are strongly anisotropic giving it a rich behavior which has been the subject of an extensive literature. It exhibits structural phase transitions in whose mechanism soft modes play an important role.[28] It therefore makes an excellent test case for our methods.

We have calculated an extensive set of phonon dispersion curves for α-quartz. Our calculations used the Perdew-Burke-Ernzerhof (PBE) variant of the GGA exchange-correlation functional.[29] The pseudopotentials were of the optimized norm-conserving variety,[30,31] generated using the LDA, and gave very well-converged results at a cutoff energy of 600 eV. A $5\times5\times4$ Monkhorst-Pack grid was used to compute the electronic Brillouin-zone integrals[24] giving essentially converged results ($|F|<5$ meV/Å and $|\sigma|<16$ MPa). The phonon calculations were carried out at the zero-pressure optimized structure with resulting lattice parameters of $a=4.940$ Å and $c=5.413$ Å and the results are plotted in Fig. 2 along with experimental results.[32,33] The agreement with experiment is reasonable, but some of the branches in the center of the frequency range are shifted to lower frequencies.

TABLE II. The Born effective charge tensors of α-quartz (units of electronic charge).

Atom	GGA			LDA		
O	−1.34	0.55	0.40	−1.29	0.46	0.26
	0.57	−2.04	−0.81	0.51	−2.01	−0.76
	0.42	−0.79	−1.74	0.32	−0.71	−1.72
Si	3.00	0.00	0.00	2.97	0.00	0.00
	0.00	3.76	0.13	0.00	3.64	0.30
	0.00	−0.15	3.48	0.00	−0.35	3.43

A detailed comparison of zone-center frequencies using both LDA and GGA with previous results is given in Table I. Our LDA results are in good agreement with earlier plane-wave calculations and with recent all-electron calculations. The agreement is less good in the case of the PBE functional, where in particular the lowest $A1$ mode drops below the E modes. Elsewhere in the spectrum discrepancies of up to 60 cm^{-1} are present. This calculation is not directly comparable with all-electron GGA results because the LDA was used to generate the pseudopotentials. This approximation makes some error, usually no greater than that due to the XC functional error, and in particular gives lattice parameters and bond lengths intermediate between LDA and consistent GGA values.[34] However, quartz frequencies are highly sensitive to crystal geometry (requiring tighter geometry convergence tolerances than usual to converge the result) due to the low-frequency rigid unit modes.[28] We suspect this to be the origin of the unusually large discrepancy observed in quartz. A definitive answer to this question will require careful testing of the accuracy with GGA-generated pseudopotentials and is beyond the scope of the present work.

We have also computed the infrared (ir) absorption spectrum of α-quartz, which is shown in Fig. 3. The intensities were computed using a spherical average approximation from the mode effective charges.

The Born effective charges and dielectric permittivity are given in Tables II and III. We find little significant difference in the values of the Born effective charges compared to either our or previous LDA calculations.[35] However, our GGA high-frequency permittivities are in excellent agreement with experiment[38] in contrast to LDA results which are 10% higher. (We have checked that the pseudopotential error in these permittivities and Born effective charges is around the

TABLE III. Low- and optical-frequency dielectric permittivities ϵ_r of α-quartz. Experimental results are from Refs. 38 and 39.

Frequency	Direction	GGA	LDA	Expt.
$\omega=0$	xx	4.427	4.803	4.42
	zz	4.632	5.029	4.60
$\omega\rightarrow\infty$	xx	2.381	2.602	2.356
	zz	2.404	2.641	2.383

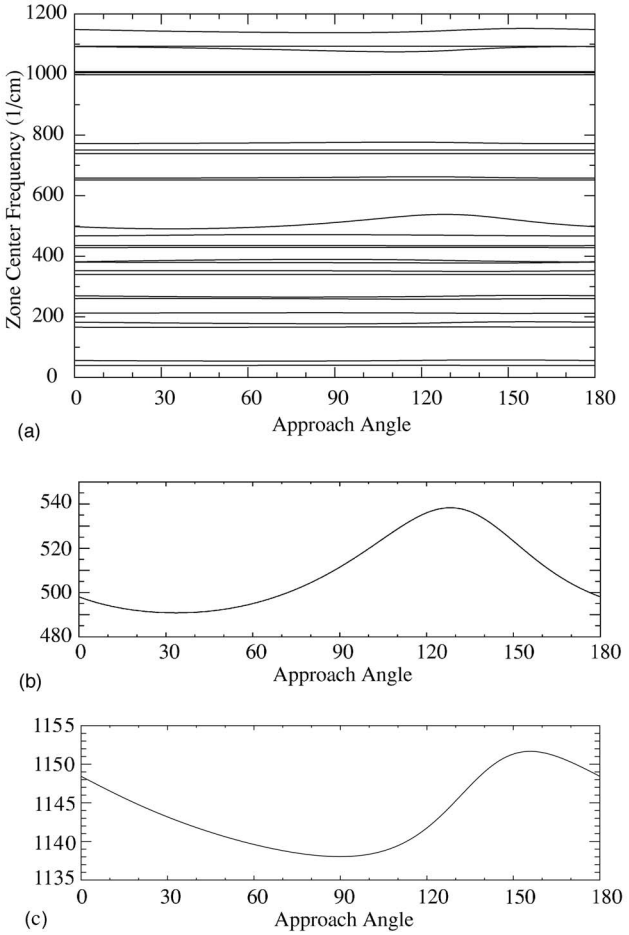

FIG. 4. The variation in zone-center frequencies for α-quartz is shown as a function of the direction from which the center of the Brillouin zone is approached. In (a) we show the variation in frequency for all modes, while in (b) and (c) we emphasize the effect by illustrating the change in two particular modes.

1% level.) In Ref. 35 agreement between LDA values and experiment was obtained only by upshifting the conduction band energies by 1.8 eV. A very similar decrease in the high-frequency dielectric permittivity was found in a recent all-electron calculation using Gaussian basis sets.[36] Given that the GGA does not correct the LDA underestimation of band gaps and that GGA dielectric permittivities for quartz are in good agreement with experiment, the earlier conclusion that the band-gap error is responsible for the overestimation of permittivities[35] is not supported.

To illustrate the directionally dependent behavior, we have determined the zone-center frequencies of α-quartz as a function of the approach of $\boldsymbol{q}$ to the Brillouin-zone center. In Fig. 4, we show the zone-center frequencies as $\boldsymbol{q}$ tends to zero from directions within the $\boldsymbol{q}=(q_x,q_y,0)$ plane, where the approach angle is measure relative to the q_x axis. As one can see, for particular modes this has a pronounced effect, and in the case of α-quartz the frequency can vary by as much as 50 wave numbers. This example highlights the need to always quote the direction with which $\boldsymbol{q}$ tends to zero when reporting the frequency of any LO mode.

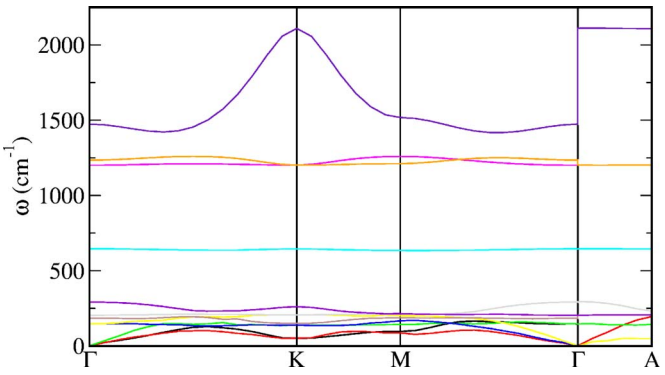

FIG. 5. (Color online) Phonon dispersion of $NaHF_2$. The hexagonal setting and its labeling scheme are assumed here.

C. Sodium hydrogen fluoride

Sodium hydrogen fluoride ($NaHF_2$) is a strongly hydrogen-bonded ionic molecular crystal, which presents a challenging test of our methods. The nature of the chemical bonds within the linear FHF^- ion is unusual and generates interesting crystal structure polymorphs and a rich phase diagram.[40] This molecular anion is highly polarizable with a significant anisotropy, which it is difficult to describe accurately using local basis-set methods.[41] Finally we will show that the LDA description of this system is grossly in error, but that the GGA results are in excellent agreement with experiment.

CASTEP calculations were performed using optimized norm-conserving pseudopotentials[30,31] which gave well-converged-results at a cutoff of 850 eV. For Na the semicore $2s$ and $2p$ electrons were treated as valence states. Brillouin-zone integration was carried out using a $5\times5\times5$ mesh according to the recipe of Monkhorst and Pack.[24] The experimental zero-pressure crystal structure of $NaHF_2$ is rhombohedral $R\bar{3}m$. An initial geometry optimization was performed to relax the structure yielding lattice constants of $a=3.538$ Å and $c=13.908$ Å compared to experimental values $a=3.474$ Å and $c=13.788$ Å.[40] The H-F bond length was 1.146 Å compared to 1.13 Å.[42] DFPT calculations were performed to compute the dynamical matrices which were diagonalized to give vibrational spectra. Electric field DFPT calculations yielded the the Born effective charges and dielectric permittivity as well as the nonanalytic corrections to the dynamical matrix at $\boldsymbol{q}=\boldsymbol{0}$. The phonon dispersion curves are plotted in Fig. 5, the Born effective charges are given in Table IV, and some selected zone-center frequencies are tabulated in Table V.

The most striking feature of the dispersion plot is the extraordinarily large LO-TO splitting observed in the highest-frequency FHF^- stretch mode of 1474 cm^{-1}. This re-

TABLE IV. The Born effective charges of $NaHF_2$.

Direction	H	F	Na
xx/yy	0.337	−0.686	1.057
zz	2.017	−1.510	1.044

TABLE V. Selected zone-center frequencies in units of cm^{-1} of $NaHF_2$ are shown and compared to experimental results, where available. ir frequencies are from Ref. 43, Raman data from Ref. 40, and inelastic neutron scattering (INS) frequencies from Ref. 44.

DFPT ($\Gamma \rightarrow K$)	DFPT ($\Gamma \rightarrow A$)	Raman	ir	INS
146.6	146.6	144.5		158
184.3	146.6			
204.4	204.4			212
646.0	646.0	630.3		635
1201.0	1201.0		1202	
1235.2	1201.0			1234
1473.9	2111.2		1550	1413

sults from a coupling of the internal FHF^- anion mode to the crystal's electrostatic field. The anomalous magnitude is in part a consequence of the very high Born charges which give rise to a large electric dipole in the distorted ion. This also accounts for the anomalously large dispersion of this mode in the (hexagonal) basal plane; internal modes ordinarily exhibit very small dispersion.

The Z_{eff} of over +2 on a hydrogen atom along the molecular axis at first seems paradoxical, as it would appear to imply that displacing the proton moves more charge than surrounds it. In fact this is easily explained. Figure 6(a) shows an isosurface of the first-order charge density associated with a displacement of the proton perpendicular and parallel to the molecular axis. It can be seen that the bulk of the charge which moves upon proton displacement actually belongs to the fluorine atoms. Also shown in Fig. 6(b) is the first-order charge density response to an applied electric field.

A final point which merits a remark here is the very large error in the phonon dispersion made by the LDA in a similar calculation. Although the lattice parameters are only slightly changed, showing the usual LDA underestimation (a =3.345 Å, c=13.656 Å) the highest branch is increased in frequency to a range of 1718–2306 cm^{-1} compared to 1473–2111 cm^{-1} using the PBE GGA. This is not simply a consequence of a grossly underestimated bond length as observed in other hydrogen-bonded systems; in this case the H-F bond length is shortened by only 0.6% to 1.140 Å.

D. (4–4′)-pentyl-cyano-biphenyl (5CB)

The 5CB molecule is the smallest that forms a liquid-crystal phase and as such has been the subject of many computational studies.[45] In studies of the liquid crystal phases it is found that small changes in the molecular structure and electronic properties strongly influence the macroscopic properties of the liquid crystal. As such, accurate knowledge of molecular properties is essential to understanding the behavior of the bulk material. For example, 5CB has a large molecular dipole moment of 6.55 D mainly due to the polar cyano group accepting electrons from π orbitals of the phenyl groups. This will create a significant internal electric field

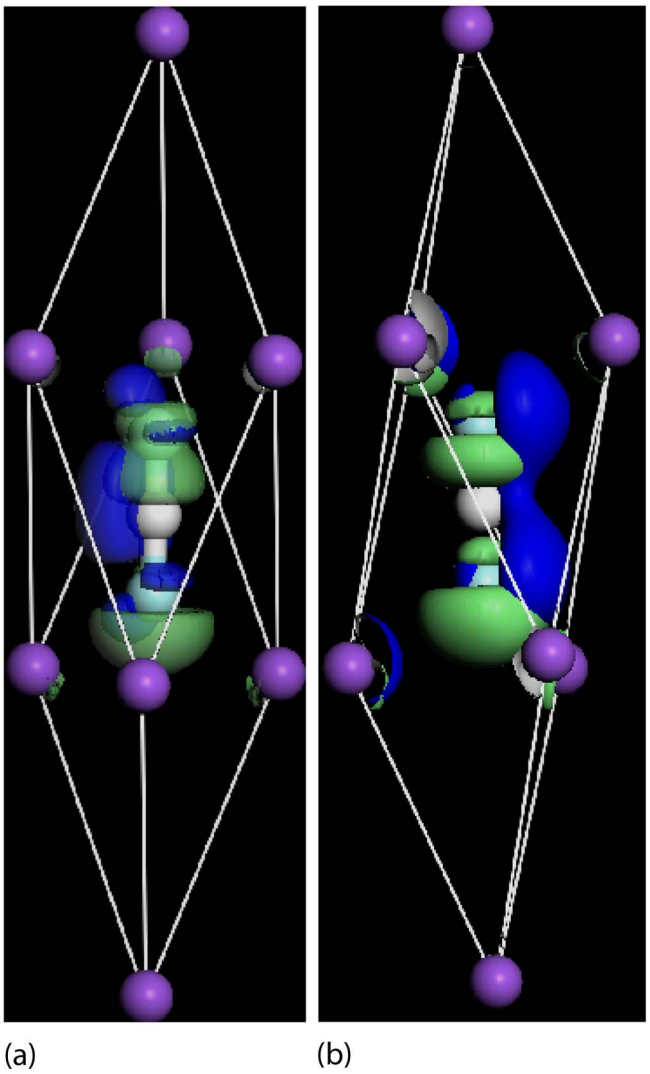

FIG. 6. (Color online) Isosurfaces of the first-order charge density in $NaHF_2$ shown for (a) an atomic perturbation associated with the H atom moving and (b) the response to an applied electric field. The light (green) isosurfaces represent motion or field parallel to the molecular axis and the dark (blue) perpendicular.

if the molecules are aligned as in a nematic phase, and will tend to polarize 5CB molecules, making the molecular polarizability an important influence on the liquid crystal structure.

Previous work on 5CB has used a finite-field, finite-difference approach to calculate the polarizability tensor.[45] That approach can be problematic; in particular Zener breakdown will eventually occur for the elongated cells necessary to model longer molecules than this. A DFPT approach is also more effective for periodic crystals which can require extremely large supercells to converge a finite-difference calculation.

Our calculation was performed using norm-conserving pseudopotentials as before and a plane-wave cutoff of 800 eV. The PBE GGA functional was used to describe the XC interactions and a geometry optimization was performed to relax the molecular structure. For this molecular case a single $\boldsymbol{k}$ point at (0,0,0) was used to sample the BZ of the

TABLE VI. The low- and high-frequency polarizabilities (in Å^3) of the 5CB molecule.

$\omega\to\infty$			$\omega=0$		
x	y	z	x	y	z
59.13	0.07	1.69	59.99	0.09	1.75
0.07	29.16	0.39	0.09	31.69	0.25
1.69	0.39	22.58	1.75	0.25	25.75

supercell. The supercell had dimensions of $30\times15\times15$ Å^3. Both lattice dynamical and electric field perturbations were calculated in order to evaluate both electronic and ionic contributions to the polarizability. These are shown in Table VI. The results agree well with previous finite-difference calculations,[45] although in the DFPT case given here, we are able to compare the difference that the ionic contributions make. We find that the most significant difference between the low- and high-frequency limits affect the transverse directions increasing the polarizability by approximately 10%.

We have also examined the effect that the electric field perturbation has on the molecule. In Fig. 7 we show the first-order charge density for an electric field perturbation applied along the length of the molecule. It is found that the response density is not localized at any particular site but distributed over the entire molecule with a slightly larger response on the cyano group at the right hand end of the figure.

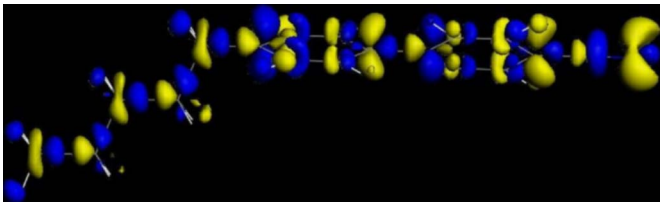

FIG. 7. (Color online) In the figure, we show an isosurface of the first-order charge density with an electric field perturbation along the length of the 5CB molecule. The light gray (yellow) shows electron enhancement and the dark gray (blue) electron depletion under application of the field.

VIII. CONCLUSIONS

In this paper, we have described the implementation details of the plane-wave density-functional methodologies not described elsewhere; in particular the terms required for the GGA response potential for a general phonon wave vector and some symmetry considerations such as an algorithm for obtaining the symmetry of the dynamical matrix. We have also compared steepest-descent and conjugate-gradient minimizers applied to the variational DFPT formalism and also the effect of several preconditioners.

These methods have been applied to three test systems, namely, α-quartz, the hydrogen-bonded $NaHF_2$ crystal, and the liquid-crystal-forming molecule 5CB. It was found that the results obtained are in excellent agreement with both experimental and other theoretical results where available.

ACKNOWLEDGMENTS

The authors wish to thank the other members of the CASTEP Developers Group (M. Segall, C. Pickard, P. Hasnip, M. Probert, and M. Payne) for their invaluable discussions throughout the development and implementation of the work presented here. We also wish to acknowledge X. Gonze for helpful technical advice. P.T. acknowledges EPSRC for financial support. Computer time was provided on the EPSRC HPCx and CSAR resources funded under the UKCP consortium Grant No. GR/N02337/01 and on CCLRCs e-Science facility.

*Electronic address: K.Refson@rl.ac.uk
†Present address: Department of Physics, University of Warwick, Coventry CV4 7AL, UK.
‡Electronic address: s.j.clark@durham.ac.uk; http://cmt.dur.ac.uk/sjc

[1] P. Hohenberg and W. Kohn, Phys. Rev. **136**, B864 (1964).
[2] W. Kohn and L. J. Sham, Phys. Rev. **140**, A1133 (1965).
[3] S. Baroni, P. Giannozzi, and A. Testa, Phys. Rev. Lett. **58**, 1861 (1987).
[4] S. Baroni, S. De Gironcoli, A. Dal Corso, and P. Giannozzi, Rev. Mod. Phys. **73**, 515 (2001).
[5] X. Gonze, Phys. Rev. A **52**, 1096 (1995).
[6] X. Gonze, Phys. Rev. B **55**, 10337 (1997).
[7] X. Gonze and C. Lee, Phys. Rev. B **55**, 10355 (1997).
[8] S. Baroni and R. Resta, Phys. Rev. B **33**, 7017 (1986).
[9] P. Giannozzi and S. Baroni, J. Chem. Phys. **100**, 8537 (1994).
[10] A. Putrino, D. Sebastiani, and M. Parrinello, J. Chem. Phys. **113**, 7102 (2000).
[11] C. J. Pickard and F. Mauri, Phys. Rev. Lett. **91**, 196401 (2003).
[12] S. J. Clark, M. D. Segall, C. J. Pickard, P. J. Hasnip, M. J. Probert, K. Refson, and M. C. Payne, Z. Kristallogr. **220**, 567 (2005).
[13] M. D. Segall, P. J. D. Lindan, M. J. Probert, C. J. Pickard, P. J. Hasnip, S. J. Clark, and M. C. Payne, J. Phys.: Condens. Matter **14**, 2717 (2002).
[14] F. Favot and A. Dal Corso, Phys. Rev. B **60**, 11427 (1999).
[15] D. Egli and S. R. Billeter, Phys. Rev. B **69**, 115106 (2004).
[16] J. A. White and D. M. Bird, Phys. Rev. B **50**, R4954 (1994).
[17] M. J. Gillan, J. Phys.: Condens. Matter **1**, 689 (1989).
[18] R. Fletcher and C. M. Reeves, Comput. J. **7**, 149 (1964).
[19] M. P. Teter, M. C. Payne, and D. C. Allan, Phys. Rev. B **40**, 12255 (1989).
[20] G. Kresse and J. Furthmüller, Phys. Rev. B **54**, 11169 (1996).
[21] A. A. Maradudin and S. H. Vosko, Rev. Mod. Phys. **40**, 1 (1968).
[22] J. L. Warren, Rev. Mod. Phys. **40**, 38 (1968).
[23] T. G. Worlton and J. L. Warren, Comput. Phys. Commun. **3**, 88 (1972).
[24] H. J. Monkhorst and J. D. Pack, Phys. Rev. B **13**, 5188 (1976).
[25] P. R. Tulip and S. J. Clark, J. Chem. Phys. **121**, 5201 (2004).
[26] P. R. Tulip and S. J. Clark, Phys. Rev. B **71**, 195117 (2005).

[27] M. A. Adams, K. Refson, and B. J. Gabrys, Phys. Chem. Chem. Phys. **7**, 3685 (2005).
[28] F. S. Tautz, V. Heine, M. T. Dove, and X. Chen, Phys. Chem. Miner. **18**, 326 (1991).
[29] J. P. Perdew, K. Burke, and M. Ernzerhof, Phys. Rev. Lett. **77**, 3865 (1996).
[30] M. H. Lee, Ph.D. thesis, Cambridge University, 1995.
[31] J. S. Lin, A. Qteish, M. C. Payne, and V. Heine, Phys. Rev. B **47**, 4174 (1993).
[32] H. G. B. Dorner and H. Rzany, J. Phys. C **13**, 6607 (1980).
[33] D. Strauch and B. Dorner, J. Phys.: Condens. Matter **5**, 6149 (1993).
[34] M. Fuchs, M. Bockstedte, E. Pehlke, and M. Scheffler, Phys. Rev. B **57**, 2134 (1998).
[35] X. Gonze, D. C. Allan, and M. P. Teter, Phys. Rev. Lett. **68**, 3603 (1992).
[36] C. M. Zicovich-Wilson, F. Pascale, C. Roetti, V. R. Saunders, R. Orlando, and R. Dovesi, J. Comput. Chem. **25**, 1873 (2004).
[37] S. E. Stein, *NIST Chemistry WebBook: NIST Standard Reference Database*, National Institute of Standards and Technology, Gaithersburg, MD, 2005, Vol. 69, http://webbook.nist.gov
[38] F. Gervais and B. Piriou, Phys. Rev. B **11**, 3944 (1975).
[39] K. F. Young and H. P. R. Fresrickse, J. Phys. Chem. Ref. Data **2**, 313 (1973).
[40] A. G. Christy, J. Haines, and S. M. Clark, J. Phys.: Condens. Matter **4**, 8131 (1992).
[41] C. L. Janssen, W. D. Allen, H. F. Schaeffer III, and J. M. Bowmen, Chem. Phys. Lett. **131**, 352 (1986).
[42] J. A. Ibers, J. Phys. (France) **25**, 474 (1964).
[43] S. Hamann and M. Linton, Aust. J. Chem. **29**, 479 (1976).
[44] P. C. H. Mitchell, S. F. Parker, A. J. Ramirez-Cuesta, and J. Tompkinson, *Vibrational Spectroscopy with Neutrons* (World Scientific, Singapore, 2005), Chap. 4, pp. 168–170.
[45] S. J. Clark, G. J. Ackland, and J. Crain, Europhys. Lett. **44**, 578 (1998).